

Equation of State table with hyperon and antikaon for supernova and neutron star merger

TUHIN MALIK ¹, SARMISTHA BANIK ¹, AND DEBADES BANDYOPADHYAY ^{2,3}

¹*Birla Institute of Technology & Sciences, Pilani
Department of Physics, Hyderabad-500078, India*

²*Saha Institute of Nuclear Physics, HBNI, 1/AF Bidhannagar, Kolkata-700064, India*

³*Frankfurt Institute for Advanced Studies (FIAS)
Ruth Moufang Strasse 1, D-60438 Frankfurt am Main, Germany*

Submitted to ApJ

ABSTRACT

We develop a new equation of state (EoS) table involving thermal (anti)kaons, Bose-Einstein condensate of K^- mesons and Λ -hyperons for core-collapse supernova and neutron star merger simulations. This EoS table is based on a finite temperature density-dependent relativistic hadron field theory where baryon-baryon interaction is mediated by scalar σ , vector ω and ρ mesons, using the parameter set DD2 for nucleons. The repulsive hyperon-hyperon interaction is mediated by an additional strange ϕ meson. The EoS for the K^- condensed matter is also calculated within the framework of relativistic mean field model, whereas the low-density, inhomogeneous matter is calculated in the extended Nuclear Statistical Equilibrium model (NSE). The EoS table is generated for a wide range of values of three parameters - baryon density (10^{-12} to $\sim 1 \text{ fm}^{-3}$), positive charge fraction (0.01 to 0.60) and temperature (0.1 to 158.48 MeV).

Keywords: Equation of state, Supernova, Neutron Stars, strange matter

1. INTRODUCTION

The study of the equation of state of matter in neutron stars has reached a high level of sophistication observationally as well as theoretically in recent years. This journey had started with the discovery of the first pulsar Hewish et al. (1968) in the year 1967. In recent years, it has got huge boost with the detection of gravitational waves in binary neutron star (BNS) merger event GW170817 Abbott et al. (2017a,b, 2018, 2019a,b,c). Parallely, the observations of heavy neutron stars led to the determination of masses $\geq 2M_{\text{solar}}$ from post Keplerian parameters using the pulsar timing technique Antoniadis et al. (2013); Cromartie et al. (2019). The simultaneous measurement of mass and radius of the x-ray powered pulsar PSR J0030+0451 is another important step forward by the Neutron Star Composition Explorer (NICER) Riley et al. (2018); Miller et al. (2019); Raaijmakers et al. (2019). All these observations are providing valuable inputs to constrain the EoS from low to very high density which could not be otherwise probed using the knowledge of laboratory experiments on nuclei and relativistic heavy ion collisions.

Observations of galactic massive pulsars PSR J0348+0432 of $2.01 \pm 0.04 M_{\text{solar}}$, PSR J0740+6620 of $2.14^{+0.10}_{-0.09} M_{\text{solar}}$ and PSR J1810+1744 of $2.13 \pm 0.04 M_{\text{solar}}$ set a lower limit on the maximum mass of neutron stars Antoniadis et al. (2013); Cromartie et al. (2019); Romani et al. (2021). On the other hand, the matter ejected in the BNS merger GW170817 was also observed across the wide electromagnetic spectrum. An upper bound on the maximum mass of neutron stars might be obtained from the electromagnetic observation of GW170817 if the remnant collapsed to a black hole. Different groups estimated the upper bound to be in the range $\sim 2.17 - 2.3M_{\text{solar}}$ Margalit & Metzger (2017); Rezzolla et al. (2018); Ruiz et al. (2018); Shibata et al. (2017, 2019). Furthermore, it was possible for the first time to extract the value of tidal deformability ($\tilde{\Lambda}$) from the gravitational waves signal of GW170817. Its range

of $70 \leq \tilde{\Lambda} \leq 720$ gives an estimate for the radius as 9-14 km for a $1.4 M_{\text{solar}}$ neutron star [Abbott et al. \(2018\)](#); [Most et al. \(2018\)](#); [Fattoyev et al. \(2018\)](#); [Raithel et al. \(2018\)](#); [De et al. \(2018\)](#); [Zhao & Lattimer \(2018\)](#); [Soma & Bandyopadhyay \(2020\)](#). The values of mass-radius of PSR J0030+0451 from two different analyses of NICER results are $1.44_{-0.14}^{+0.15} M_{\text{solar}}$ - $13.02_{-1.06}^{+1.24}$ km and $1.34_{-0.16}^{+0.15} M_{\text{solar}}$ - $12.71_{-1.19}^{+1.14}$ km [Miller et al. \(2019\)](#); [Riley et al. \(2018\)](#). Another compact binary coalescence event GW190814 involving a black hole of $23.2_{1.0}^{+1.1} M_{\text{solar}}$ and a compact object of $2.59_{0.9}^{+0.8} M_{\text{solar}}$ had been reported recent [Abbott et al. \(2020\)](#). This event has generated a debate whether the secondary mass makes the compact object the heaviest neutron star or a lightest black hole. The observed values of masses and radii are stringent probes of the EoS of neutron star matter. Theoretical models of EoS should be compatible with these observations.

The theoretical modeling of EoS has undergone a sea of changes over the past several years. Traditional EoS models are based on two-body plus three-body interactions in non-relativistic approaches and the strong interaction Lagrangian in relativistic field theoretic approaches [Lattimer & Swesty \(1991\)](#); [Shen et al. \(1998\)](#). Furthermore, compositions of matter are assumed in both types of models. Recently, large numbers of EoSs were constructed by adopting phenomenological Skyrme interaction or nucleon-nucleon chiral potentials for the low density; and perturbative Quantum Chromodynamics for asymptotically high density regimes. The EoS in the intermediate density regime is connected to EoSs at two extreme densities either by polytropes or just demanding the causality and monotonicity [Hebeler et al. \(2013\)](#); [Kurkela et al. \(2014\)](#); [Most et al. \(2018\)](#); [Oter et al. \(2019\)](#). However, such EoS models do not assume any kind of composition of matter in the intermediate density regime which plays the most important role for masses and radii of neutron stars.

Traditional models of EoS are widely used in numerical relativity simulations of compact astrophysical objects. Our motivation in this work is to compute an EoS including strange matter within the framework of relativistic field theoretical models to be used as an input in core collapse supernova (CCSN) and neutron star merger simulations.

A large set of EoSs with and without strange matter such as hyperon, antikaon condensed or quark matter are already available for CCSN and neutron star merger simulations [Hempel & Schaffner-Bielich \(2010\)](#); [Raduta & Gulminelli \(2010\)](#); [Shen et al. \(2010, 2011a,b\)](#); [Fischer et al. \(2011\)](#); [Blinnikov et al. \(2011\)](#); [Hempel et al. \(2012\)](#); [Steiner et al. \(2013\)](#); [Buyukcizmeci et al. \(2013b\)](#); [Typel et al. \(2013\)](#); [Fischer et al. \(2014\)](#); [Togashi et al. \(2014\)](#); [Constantinou et al. \(2014\)](#); [Banik et al. \(2014\)](#); [Oertel et al. \(2017\)](#); [Malik et al. \(2021\)](#). The EoS tables with nucleons-only matter satisfy the $2 M_{\text{solar}}$ lower bound on the maximum mass of neutron stars. However, many EoSs with hyperons or quarks used in CCSN simulations do not conform to the lower bound on the maximum mass [Ishizuka et al. \(2008\)](#); [Nakazato et al. \(2008\)](#); [Sagert et al. \(2009\)](#); [Sumiyoshi et al. \(2009\)](#); [Shen et al. \(2011c\)](#); [Nakazato et al. \(2012\)](#); [Oertel et al. \(2012\)](#); [Peres et al. \(2013\)](#); [Banik \(2014\)](#). Keeping this in mind, we constructed an EoS table including Λ hyperons which is compatible with $2 M_{\text{solar}}$ neutron stars [Banik et al. \(2014\)](#). This EoS, known as BHBA ϕ , is being widely used in CCSN [Char et al. \(2015\)](#) and BNS merger simulations [Radice et al. \(2018\)](#). It has been long debated that the Bose-Einstein condensate of negatively charged kaons might appear in dense matter [Kaplan & Nelson \(1986\)](#); [Knorren et al. \(1995\)](#). This idea was extended to understand the non-observation of a neutron star in SN1987A [Bethe & Brown \(1995\)](#). There was no EoS table involving an antikaon condensate in nuclear matter before our very recent work on this problem [Malik et al. \(2021\)](#). We did not consider the appearance of hyperons along with the antikaon condensate in the previous work. The early appearance of hyperons would delay the onset of Bose-Einstein condensate of antikaons in dense matter or vice versa. It is worth investigating how one form of strange matter behaves in presence of another. This motivates us to investigate this issue and extend our hyperon EoS BHBA ϕ to include the Bose-Einstein condensate of K^- mesons fulfilling most updated information on neutron stars.

The paper is organised as follows. In Section 2, the hadronic field theory models of EoSs at zero and finite temperatures are described. The results of our calculation are discussed in Section 3. Section 4 contains the summary and conclusions.

2. THE MODEL

2.1. Hadronic Model

The baryonic matter is described within the framework of the density-dependent model adopting the relativistic mean field (RMF) approximation. The baryon-baryon interaction is mediated by σ , ω , ρ and ϕ mesons. However, nucleons do not couple to ϕ mesons, they account for the repulsive hyperon-hyperon interaction. The Lagrangian density is given by [Typel et al. \(2010\)](#); [Banik et al. \(2014\)](#):

$$\begin{aligned} \mathcal{L} = & \sum_{B=N,\Lambda} \bar{\Psi}_B (i\gamma_\mu \partial^\mu - m_B + g_{\sigma B} \sigma - g_{\omega B} \gamma_\mu \omega^\mu - g_{\rho B} \gamma_\mu \boldsymbol{\tau}_B \cdot \boldsymbol{\rho}^\mu - g_{\phi B} \gamma_\mu \phi^\mu) \Psi_B \\ & + \frac{1}{2} (\partial_\mu \sigma \partial^\mu \sigma - m_\sigma^2 \sigma^2) - \frac{1}{4} \omega_{\mu\nu} \omega^{\mu\nu} + \frac{1}{2} m_\omega^2 \omega_\mu \omega^\mu - \frac{1}{4} \rho_{\mu\nu} \cdot \rho^{\mu\nu} + \frac{1}{2} m_\rho^2 \rho_\mu \cdot \rho^\mu - \frac{1}{4} \phi_{\mu\nu} \phi^{\mu\nu} + \frac{1}{2} m_\phi^2 \phi_\mu \phi^\mu, \end{aligned} \quad (1)$$

where Ψ_B denotes the isospin multiplets for baryons B, m_B 's being their bare masses, and $\boldsymbol{\tau}_B$, the isospin operator. The density dependent meson-nucleon couplings are denoted by g_{xB} with $x = \sigma, \omega$, and ρ meson fields. The vector meson field strength tensors are particularly represented by $x^{\mu\nu} = \partial^\mu x^\nu - \partial^\nu x^\mu$. In the mean field approximations, meson fields are replaced by their expectation values $\langle x \rangle$. Only the time-like components of vector fields and the third isospin component of the ρ field survive in a uniform and static matter. They are denoted by $\sigma, \omega_0, \rho_{03}$ and ϕ_0 and are obtained by solving the meson field equations in the RMF approximation,

$$m_\sigma^2 \sigma = \sum_B g_{\sigma B} \bar{\psi}_B \psi_B, \quad m_\omega^2 \omega_0 = \sum_B g_{\omega B} \bar{\psi}_B \gamma_0 \psi_B, \quad m_\rho^2 \rho_{03} = \frac{1}{2} \sum_B g_{\rho B} \bar{\psi}_B \gamma_0 \boldsymbol{\tau}_{3B} \psi_B, \quad m_\phi^2 \phi_0 = \sum_B g_{\phi B} \bar{\psi}_B \gamma_0 \psi_B.$$

The grand-canonical thermodynamic potential per unit volume of the hadronic phase is given by Banik et al. (2014); Soma & Bandyopadhyay (2020)

$$\begin{aligned} \frac{\Omega}{V} = & \frac{1}{2} m_\sigma^2 \sigma^2 - \frac{1}{2} m_\omega^2 \omega_0^2 - \frac{1}{2} m_\rho^2 \rho_{03}^2 - \frac{1}{2} m_\phi^2 \phi_0^2 - \Sigma^r \sum_{B=n,p,\Lambda} n_B \\ & - 2T \sum_{B=n,p,\Lambda} \int \frac{d^3k}{(2\pi)^3} [\ln(1 + e^{-\beta(E^* - \nu_B)}) + \ln(1 + e^{-\beta(E^* + \nu_B)})], \end{aligned} \quad (2)$$

where the temperature is defined as $\beta = 1/T$ and $E^* = \sqrt{(k^2 + m_B^{*2})}$.

The number densities and scalar number densities of baryon B are $n_B = \langle \bar{\psi}_B \gamma_0 \psi_B \rangle$, and $n_B^S = \langle \bar{\psi}_B \psi_B \rangle$ respectively, and at finite temperature (T) are given by,

$$n_B = 2 \int \frac{d^3k}{(2\pi)^3} \left(\frac{1}{e^{\beta(E^* - \nu_B)} + 1} - \frac{1}{e^{\beta(E^* + \nu_B)} + 1} \right), \quad (3)$$

$$n_B^S = 2 \int \frac{d^3k}{(2\pi)^3} \frac{m_B^*}{E^*} \left(\frac{1}{e^{\beta(E^* - \nu_B)} + 1} + \frac{1}{e^{\beta(E^* + \nu_B)} + 1} \right). \quad (4)$$

Here the effective nucleon mass is $m_B^* = m_B - g_{\sigma B} \sigma$. The chemical potential is given by $\mu_B = \nu_B + g_{\omega B} \omega_0 + g_{\rho B} \boldsymbol{\tau}_{3B} \rho_{03} + g_{\phi B} \phi_0 + \Sigma^r$, where the rearrangement term Σ^r takes care of many-body effects in nuclear interaction Typel et al. (2010); Banik et al. (2014). It arises due to the density-dependence of the couplings and is expressed as

$$\Sigma^r = \sum_B \left[-\frac{\partial g_{\sigma B}}{\partial n_B} \sigma n_B^S + \frac{\partial g_{\omega B}}{\partial n_B} \omega_0 n_B + \frac{\partial g_{\rho B}}{\partial n_B} \boldsymbol{\tau}_{3B} \rho_{03} n_B + \frac{\partial g_{\phi B}}{\partial n_B} \phi_0 n_B \right]. \quad (5)$$

The pressure is calculated from the grand-canonical thermodynamic potential per unit volume as $P = -\Omega/V$ as given by Eq.(2) and includes the rearrangement term.

However, the energy density does not explicitly contain the rearrangement term, as evident from its expression,

$$\epsilon_B = \frac{1}{2} m_\sigma^2 \sigma^2 + \frac{1}{2} m_\omega^2 \omega_0^2 + \frac{1}{2} m_\rho^2 \rho_{03}^2 + \frac{1}{2} m_\phi^2 \phi_0^2 + 2 \sum_{B=N,\Lambda} \int \frac{d^3k}{(2\pi)^3} E^* \left(\frac{1}{e^{\beta(E^* - \nu_B)} + 1} + \frac{1}{e^{\beta(E^* + \nu_B)} + 1} \right). \quad (6)$$

The rearrangement term not only accounts for the energy-momentum conservation but also the thermodynamic consistency of the system. The energy density and pressure are related through Gibbs-Duhem relation i.e. $\mathcal{S}_B = \beta (\epsilon_B + P_B - \sum_B \mu_B n_B)$, where, \mathcal{S}_B is the entropy density of baryon B.

2.2. Model for antikaons

Kaon-nucleon interaction is considered in the same footing as the nucleon-nucleon interaction in Eq.(1). The Lagrangian density for (anti)kaons in the minimal coupling scheme is Glendenning & Schaffner-Bielich, (1999); Pons et al. (2000); Banik & Bandyopadhyay, (2001); Banik. et al. (2008); Char & Banik, (2014),

$$\mathcal{L}_K = D_\mu^* \bar{K} D^\mu K - m_K^{*2} \bar{K} K, \quad (7)$$

where K and \bar{K} denote kaon and (anti)kaon doublets; the covariant derivative is $D_\mu = \partial_\mu + ig_{\omega K} \omega_\mu + ig_{\rho K} \tau_K \cdot \rho_\mu + ig_{\phi K} \phi_\mu$ and the effective mass of antikaon is $m_K^* = m_K - g_{\sigma K} \sigma$. Meson fields are modified in the presence of K^- condensate Glendenning & Schaffner-Bielich, (1999); Banik & Bandyopadhyay, (2001) and are obtained solving the following equations:

$$\begin{aligned} m_\sigma^2 \sigma &= \sum_B g_{\sigma B} n_B^S + \sum_K g_{\sigma K} n_K, & m_\omega^2 \omega_0 &= \sum_B g_{\omega B} n_B - \sum_K g_{\sigma K} n_B, \\ m_\rho^2 \rho_{03} &= \frac{1}{2} \sum_B g_{\rho B} \tau_{3B} n_B + \sum_K g_{\sigma K} n_K \tau_{3K}, & m_\phi^2 \phi_0 &= \sum_B g_{\phi B} n_B - \sum_K g_{\sigma K} n_K. \end{aligned}$$

The thermodynamic potential for (anti)kaons is given by Pons et al. (2000); Banik. et al. (2008),

$$\frac{\Omega_K}{V} = T \int \frac{d^3 k}{(2\pi)^3} [\ln(1 - e^{-\beta(\omega_{K^-} - \mu)}) + \ln(1 - e^{-\beta(\omega_{K^+} + \mu)})], \quad (8)$$

where the in-medium energies of K^\pm mesons are given by

$$\omega_{K^\pm} = \sqrt{(k^2 + m_K^{*2})} \pm \left(g_{\omega K} \omega_0 + \frac{1}{2} g_{\rho K} \rho_{03} + g_{\phi K} \phi_0 \right). \quad (9)$$

The chemical potentials of nucleons are related to that of K^- mesons by $\mu = \mu_n - \mu_p$ Pons et al. (2000). For s-wave ($\mathbf{k} = 0$) condensation, the momentum dependence vanishes in ω_{K^\pm} . The in-medium energy of K^- condensate decreases from its vacuum value m_K as the meson fields build up with increasing density. The K^- condensate appears in the system as ω_{K^-} equals to its chemical potential i.e. $\mu = \omega_{K^-} = m_K^* - g_{\omega K} \omega_0 - \frac{1}{2} g_{\rho K} \rho_{03} - g_{\phi K} \phi_0$. This is the threshold condition for K^- condensation. Incidentally, the threshold condition for K^+ condition $\mu = \omega_{K^+}$ is never attained because of the repulsive nature of K^+ -nucleon interaction. We calculate the pressure due to thermal (anti)kaons using $P_K = -\Omega_K/V$. K^- condensate does not contribute to pressure. The energy density of (anti)kaons is due to the condensate as well as the thermal (anti)kaons and is given by,

$$\epsilon_K = m_K^* n_K^C + \left(g_{\omega K} \omega_0 + \frac{1}{2} g_{\rho K} \rho_{03} + g_{\phi K} \phi_0 \right) n_K^T + \int \frac{d^3 k}{(2\pi)^3} \left(\frac{\omega_{K^-}}{e^{\beta(\omega_{K^-} - \mu)} - 1} + \frac{\omega_{K^+}}{e^{\beta(\omega_{K^+} + \mu)} - 1} \right). \quad (10)$$

The thermodynamic quantities-entropy density, energy density, pressure, chemical potential and number density are related to each other through $\mathcal{S}_K = \beta(\epsilon_K + P_K - \mu n_K)$. The entropy per baryon is given by $s = \mathcal{S}/n_B$, where n_B is the total baryon density. The total (anti)kaon number density (n_K) is given by, $n_K = n_K^C + n_K^T$, where, n_K^C and n_K^T are the K^- condensate and thermal (anti)kaon density respectively. They are given by,

$$\begin{aligned} n_K^C &= 2 \left(\omega_{K^-} + g_{\omega K} \omega_0 + \frac{1}{2} g_{\rho K} \rho_{03} + g_{\phi K} \phi_0 \right) \bar{K} K = 2m_K^* \bar{K} K, \\ n_K^T &= \int \frac{d^3 k}{(2\pi)^3} \left(\frac{1}{e^{\beta(\omega_{K^-} - \mu)} - 1} - \frac{1}{e^{\beta(\omega_{K^+} + \mu)} - 1} \right). \end{aligned} \quad (11)$$

2.3. Parameters of the DD2 model

The nucleon-meson couplings depend on the density through $g_{\alpha B}(n_B) = g_{\alpha B}(n_0) f_\alpha(x)$ where $x = n_B/n_0$, and

$$f_\alpha(x) = a_\alpha \frac{1 + b_\alpha(x + d_\alpha)^2}{1 + c_\alpha(x + d_\alpha)^2}$$

for $\alpha = \omega, \sigma$ Typel & Wolter (1999); Typel et al. (2010). An exponential density-dependence is assumed for the isovector meson ρ i.e. $f_\alpha(x) = \exp[-a_\alpha(x - 1)]$, as their couplings decrease at higher densities Typel & Wolter (1999).

The DD2 parameter set of nucleon-meson couplings used in the calculation, results in the saturation properties of symmetric nuclear matter such as $n_0 = 0.149065 \text{ fm}^{-3}$, binding energy per nucleon 16.02 MeV, incompressibility 242.7 MeV, symmetry energy 31.67 MeV and its slope coefficient 55.03 MeV [Typel et al. \(2010\)](#); [Fischer et al. \(2014\)](#).

The system is populated with Λ 's when the chemical equilibrium condition $\mu_n = \mu_\Lambda$ is met. The density-dependent Λ -vector meson hyperon vertices are obtained from the SU(6) symmetry of the quark model [Dover & Gal \(1985\)](#); [Schaffner & Mishustin \(1996\)](#).

$$g_{\omega\Lambda} = \frac{2}{3}g_{\omega N}, \quad g_{\rho\Lambda} = 0, \quad g_{\phi\Lambda} = -\frac{\sqrt{2}}{3}g_{\omega N}.$$

On the other hand, the Λ hyperon - scalar meson couplings are obtained from the hypernuclei data. We consider Λ hyperon potential depth $U_\Lambda^N = g_{\omega\Lambda}\omega_0 - g_{\sigma\Lambda}\sigma_0 + \Sigma^r = -30 \text{ MeV}$ in normal nuclear matter [Millener et al. \(1988\)](#); [Schaffner et al. \(1992\)](#); [Mares et al. \(1995\)](#) and the ratio of $g_{\sigma\Lambda}$ to $g_{\sigma N}$ is 0.62008.

However, kaon-meson couplings are not density-dependent. The kaon-vector meson coupling constants are also estimated exploiting the quark model and isospin counting rule i.e. $g_{\omega K} = \frac{1}{3}g_{\omega N}$ and $g_{\rho K} = g_{\rho N}$ [Schaffner & Mishustin \(1996\)](#); [Banik & Bandyopadhyay, \(2001\)](#). The scalar coupling constant is determined from the real part of K^- optical potential $U_{K^-} = -g_{\sigma K}\sigma_0 - g_{\omega K}\omega_0 + \Sigma^r$ at the saturation density, for which an appropriate value of -120 MeV is considered in this work such that the cold beta-equilibrated EoS is compatible with 2 M_{Solar} neutron stars. The K^- optical potential could actually range from -60 MeV to -200 MeV as indicated by the unitary chiral model calculations and phenomenological fit to kaonic atom data [Friedman et al. \(1994, 1999\)](#); [Tólos et al. \(2006\)](#); [Tolos & Fabbietti \(2020\)](#).

2.4. Matching with the low density EoS

The inhomogeneous nuclear matter at low temperatures ($\sim 10 \text{ MeV}$) and the sub-saturation density, is composed of light and heavy nuclei along with unbound nucleons. In this case, we use the HS(DD2) EoS described within the extended Nuclear Statistical Equilibrium(NSE) Model of Hempel & Schaffner-Bielich [Hempel & Schaffner-Bielich \(2010\)](#). It is expected that hyperons and/or (anti)kaons would not appear at the low densities and low temperatures. In this situation, we compare the free energy per baryon at fixed n_B , T and Y_q of the data of our uniform EoS table with those of the HS(DD2) EoS table. If the free energy of HS(DD2) table is less than that our EoS table, we replace the corresponding data of the latter with those of the former to get the final EoS table with Λ hyperons and (anti)kaons. Furthermore, we impose the condition that hyperons and (anti)kaons are considered only when their fractions are $> 10^{-5}$ to avoid unphysical situations and ensure a smooth transition between low and high densities. Henceforth we call this merged EoS table ¹ with Λ -hyperon and K^- as BHBAK $^-$ ϕ EoS. Incidentally we generated a similar EoS table (BHBA ϕ) with Λ -hyperons following the similar procedure [Banik et al. \(2014\)](#).

2.5. Accuracy and Consistency of the EoS table

The following consistency checks on the EoS table are performed. Thermodynamic consistency is achieved by the condition:

$$f = \mu_n n_n + \mu_p n_p + \mu_\Lambda n_\Lambda + \mu n_K - P,$$

where $f = \epsilon - TS$.

The modulus of the relative thermodynamic accuracy in this EoS table is given by

$$\Delta = \frac{TS - P + \mu_n n_n + \mu_p n_p + \mu_\Lambda n_\Lambda + \mu n_K}{\epsilon} - 1 \sim 10^{-7}.$$

Sum rule of particle fractions (X_i) is satisfied by the EoS table given by

$$X_n + X_p + X_s + X_A + X_\Lambda = 1.$$

Finally, the EoS table fulfills the thermodynamic stability criteria:

$$\frac{dS}{dT} > 0, \quad \frac{dP}{dn_B} > 0.$$

¹ <https://universe.bits-pilani.ac.in/Hyderabad/sbanik/EoS>

3. RESULTS AND DISCUSSION

The EoS table with thermal (anti)kaons and K^- condensate are generated using the DD2 parameter set and $U_{K^-} = -120$ MeV for baryon densities ($n_B = 10^{-12}$ to $\sim 1 fm^{-3}$), temperatures ($T = 0.1$ to 158.48 MeV) and positive charge fractions $Y_q(n_B) = n_p - n_K$ ($Y_q = 0.01$ to 0.60). Grid spacing for baryon density is $\Delta \log_{10}(n_B) = 0.04$; for temperature $\Delta \log_{10}(T) = 0.04$ and for positive charge fraction $\Delta Y_q = 0.01$. The EoS table consists of 301 baryon density points, 81 temperatures and 60 positive charge fractions i.e. total one million data points.

Before describing the thermodynamic quantities in BHBAK $^- \phi$ EoS table, we discuss the β -equilibrated matter relevant to cold neutron stars. We generate the EoS of neutron stars by imposing charge neutrality with the inclusion of electrons and the β -equilibrium condition without neutrinos at temperature $T = 0$. In Fig.1a, various particle fractions are plotted as a function of baryon number density. The NS core contains a high neutron fraction. The proton fraction increases monotonically as baryon density increases. The positive charges of protons are balanced by negative charges of electrons. Λ -hyperons appear at $\sim 2.2n_B$ followed by the K^- condensate. The early appearance of Λ hyperons makes the EoS softer delaying the appearance of the antikaon condensate. The K^- fraction in the condensate abundance reaches a considerable fraction at $3.5n_B$. As soon as K^- appears, the e^- fraction drops and the charge neutrality is totally taken care off by the negatively charged condensate at higher density. On the other hand the population of neutrons is arrested due to the accumulation of more Λ s at higher density.

The mass-radius relationship of the sequence of neutron stars is shown in Fig.1b for HS(DD2), HS(DD2) K^- , BHBA ϕ and BHBAK $^- \phi$ EoS. The solid line (green) represents the nucleons-only neutron star. On the other hand, dotted (magenta), dashed-dotted (blue) and dashed (red) lines represent neutron stars with additional K^- condensate only, Λ -hyperons only, and both Λ -hyperons and K^- condensate respectively. The maximum masses for the four EoSs are 2.42 , 2.24 , 2.1 and $2.05 M_{solar}$, their corresponding radii being 11.89 , 12.0 , 11.58 , 11.62 km respectively. The Λ -hyperons make the EoS softer, resulting in a smaller as well as lighter maximum mass neutron star compared with that of the nucleons-only HS(DD2) EoS. The maximum mass is further lowered in the presence of K^- condensate. It is to be noted that the masses are well within the observational benchmark of measured $2 M_{solar}$ neutron stars [Antoniadis et al. \(2013\)](#); [Cromartie et al. \(2019\)](#).

We now move on to the results relevant to the BHBAK $^- \phi$ EoS table for supernova and NS merger simulations. Fig. 2 exhibits the composition of supernova matter as a function of baryon mass density for $T = 1, 50,$ and 100 MeV and $Y_q = 0.1, 0.3,$ and 0.5 . Number densities of various particles, such as light ($Z \leq 5$), heavy nuclei ($Z \geq 6$), neutrons, protons, Λ -hyperon and antikaons, both thermal and condensate are plotted. The heavy nuclei exist only at the low temperature and low density non-uniform matter. The light nuclei on the other hand appear in the low density region only for $T = 50$ MeV and higher charge fractions, as evident from the middle panel of Fig. 2. At very high temperatures > 48 MeV, nuclei do not appear. Furthermore, nuclei dissolve into their fundamental constituents around normal nuclear matter density and form a uniform matter of neutrons and protons. The Λ -hyperons appear with significant abundance ($> 10^{-5}$) at higher density at the cost of neutrons. Higher the temperature, lower is their threshold density. However the population fractions of baryons do not differ with temperature at relatively higher density. Next we focus on the (anti)kaon number density. The antikaon condensate does not appear at all for a system with higher charge fraction Y_q . Even for $Y_q = 0.1$, its threshold is shifted towards higher density, and it fails to appear at $T = 100$ MeV. This may be attributed to the abundance of thermal kaons at higher temperatures, which cannot be traced at low temperature regime. In fact above the critical temperature, the condensate disappears producing thermal (anti)kaons. Nevertheless, Λ -hyperons also play a dominant role. We have reported in an earlier work with (anti)kaons, but no hyperons, the density of K^- mesons in the condensate even dominates over that of thermal (anti)kaons (n_K^T) at $T = 50$ MeV for $Y_q = 0.1$ and 0.3 [Malik et al. \(2021\)](#). Here this trend is noted only for $Y_q = 0.1$. Thus we conclude that the Λ -hyperons delay or do not allow the K^- condensate to appear in the system, more so at higher Y_q .

We have studied various thermodynamic observables such as free energy per baryon, entropy per baryon and pressure as a function of baryon mass density. In all following figures, we only show the hadronic contribution and plot them for various regimes of temperatures, $T = 1, 50,$ and 100 MeV and positive charge fractions, $Y_q = 0.1, 0.3,$ and 0.5 . Free energy per baryon with respect to the arbitrary value of $m_0 = 938$ MeV is plotted for BHBAK $^- \phi$ EoS in Fig. 3 as a function of mass density (in red dashed line). The results for nucleons-only HS(DD2) EoS (green solid) and BHBA ϕ (black solid line) EoSs are also drawn for comparison. At lower densities, there is practically no difference between the results of nuclear and strange matter for different situations considered. A slight difference is observed at higher density for $T = 1$ and 50 MeV, when the strange particles appear. The difference is quite prominent at $T = 100$ MeV, owing to appearance of thermal (anti)kaons at a lower density along with the Λ s. If we compare the the right-most

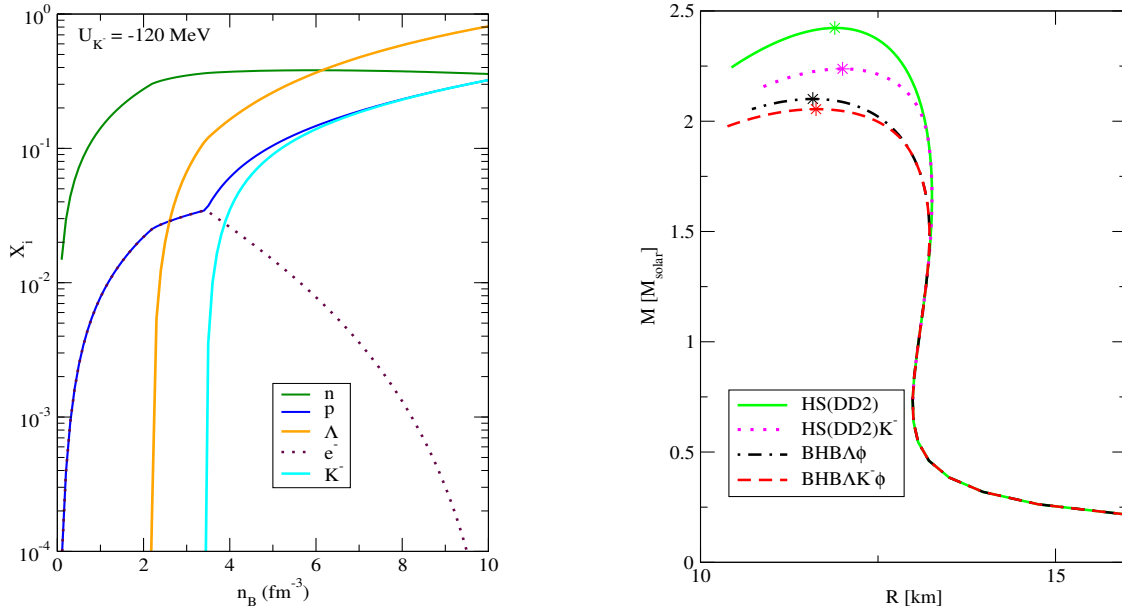


Figure 1. Properties of β -equilibrated cold neutron star: a) Particle fractions of various species in a β -equilibrated cold NS are plotted as a function of baryon number density for BHB $\Lambda K^- \phi$ EoS b) Masses of the NS sequence are plotted as a function of radius for nucleonic and strange EoSs. Stars mark the maximum mass configurations.

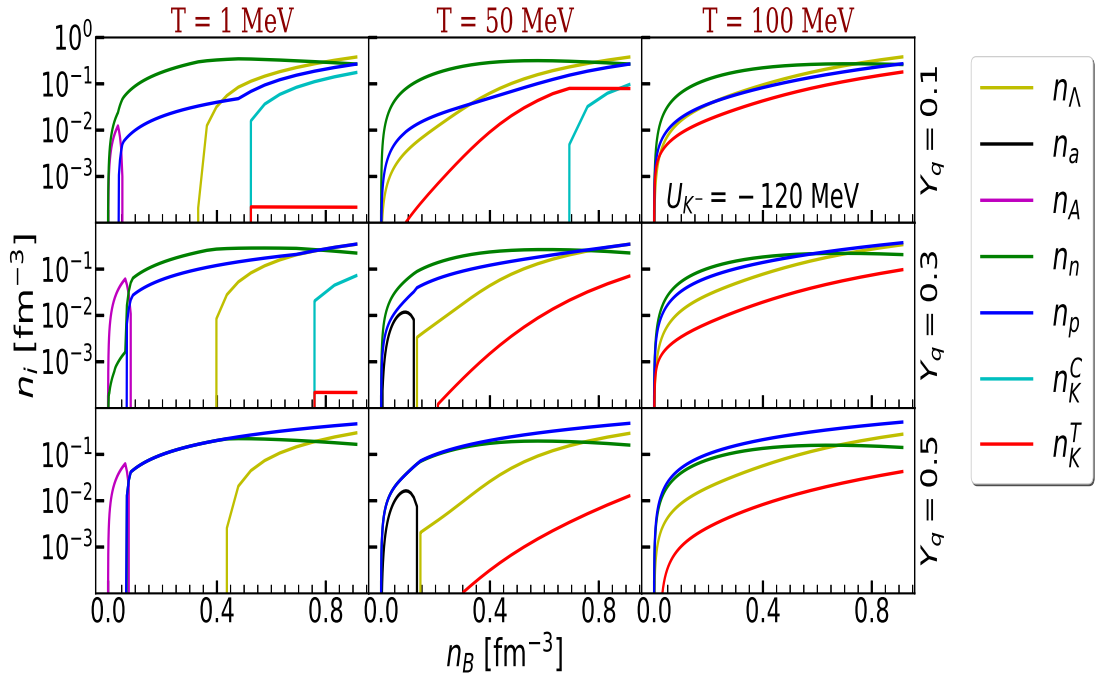


Figure 2. Number densities of different particle species, such as light & heavy nuclei, neutrons, protons and antikaons, both thermal and condensate, Λ -hyperons as a function of baryon number density for $T=1, 50, 100$ MeV and $Y_q = 0.1, 0.3, 0.5$.

panel of Fig. 3 at $T=100$ MeV, the effect of thermal (anti)kaons become evident. The difference between free energy of nuclear and strange matter is noticed to disappear apparently for $Y_q=0.5$. This may be attributed to the dissolution of the condensate with the production of thermal (anti)kaons at comparatively higher density. Also its abundance is observed to be relatively small compared to the matter with lower Y_q .

The pressure is plotted in Fig. 4, as a function of baryon mass density. Just like the free energy case, we find the nuclear and strange EoSs do not show any difference at low densities for the different values of temperature and

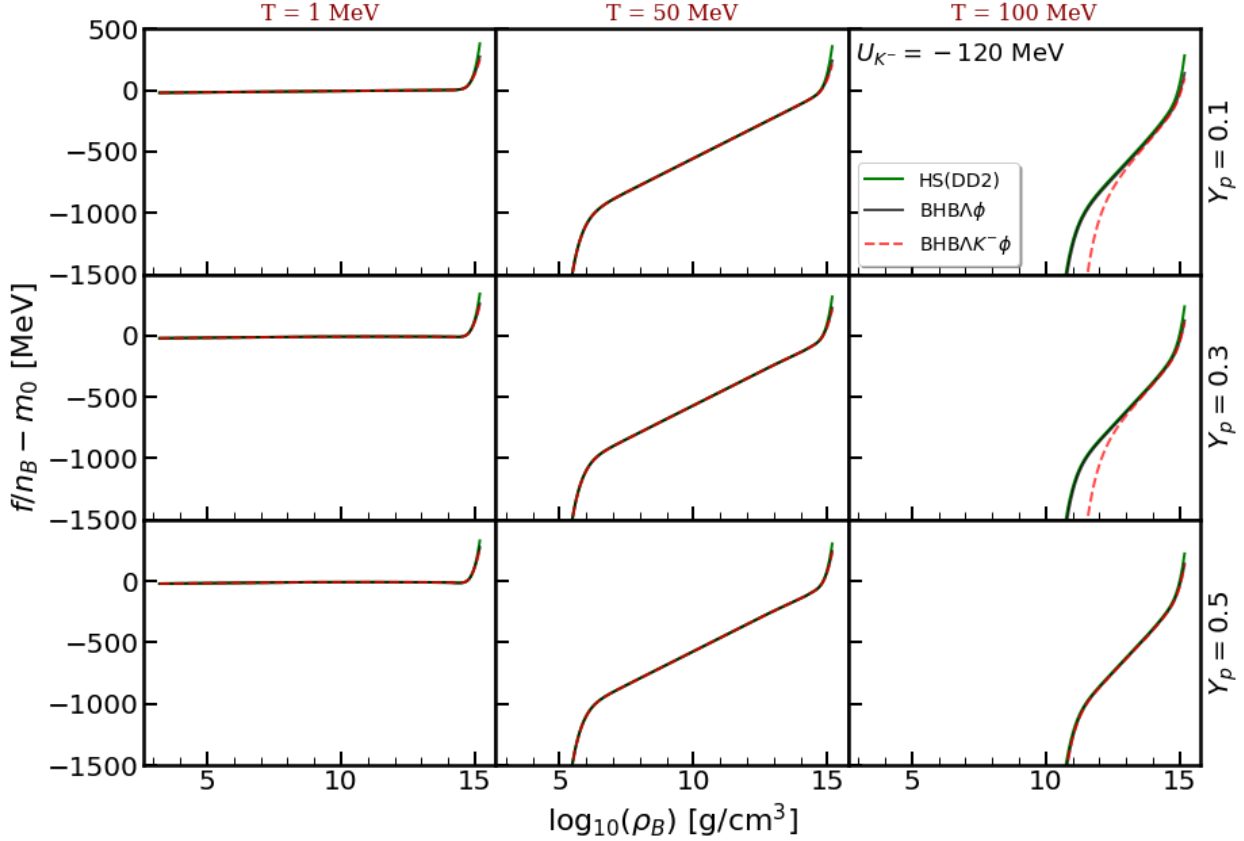


Figure 3. Free energy per baryon with respect to $m_0 = 938$ MeV is plotted as a function of baryon mass density for temperatures $T = 1, 50, 100$ MeV and positive charge fraction $Y_q = 0.1, 0.3$ and 0.5 . Results from the nucleonic EoS table HS(DD2) (green) and strange EoS tables BHBA ϕ (black) BHBA $K^- \phi$ (red-dashed) are shown here

positive charge fractions considered here. However, at the higher density the exotic particles appear, which clearly makes the BHBA $K^- \phi$ EoS softer compared to the HS(DD2) and BHBA ϕ EoSs. The high density portion is zoomed in the inset box for $Y_q = 0.1$ and $T=1$ MeV to highlight this difference. A kink in pressure is observed at $\sim 10^{10}$ g/cm^3 for $T=100$ MeV and $Y_q = 0.1$ and 0.3 , which is due to significant contribution of thermal K^- mesons to the pressure. There is no kink or jump in pressure when Λ s appear in the system indicating a smooth transition from nuclear to hyperon matter.

In Fig. 5 the entropy per baryon as a function of baryon mass density for the same set of values of temperatures and positive charge fractions are plotted. Here also, the effect of strange particles become evident in the high density region. The kinks at low densities and temperatures originate from changes in the nuclear composition which are related to nuclear shell effects, whereas the kinks at higher densities mark the appearance of exotic particles. The difference between the three EoSs is prominent only at higher density for $T=50$ MeV. However the large fraction of thermal (anti)kaons at low density does make a significant effect at $T=100$ MeV for $Y_q=0.1$ and 0.3 . This effect is blurred at $Y_q=0.5$, as the thermal (anti)kaons appear at higher density and the BHBA $K^- \phi$ curve deviates from HS(DD2) and BHBA ϕ EoSs at the higher density end.

Finally in Fig. 6, we plot the phase diagram, i.e. the temperature versus baryon density for $Y_q=0.1$ and 0.3 . The shaded regions below the solid lines represent the kaon condensed phase in the presence of hyperons. The solid line demarcates the hyperon matter phase from the condensate phase for a particular value of Y_q and denotes the critical temperature of kaon condensation at each density point. At higher Y_q , the condensate appears at higher density. Condensate may not appear at all if the temperature of the system is high, as was seen in Fig. 2. Malik et al. (2021)

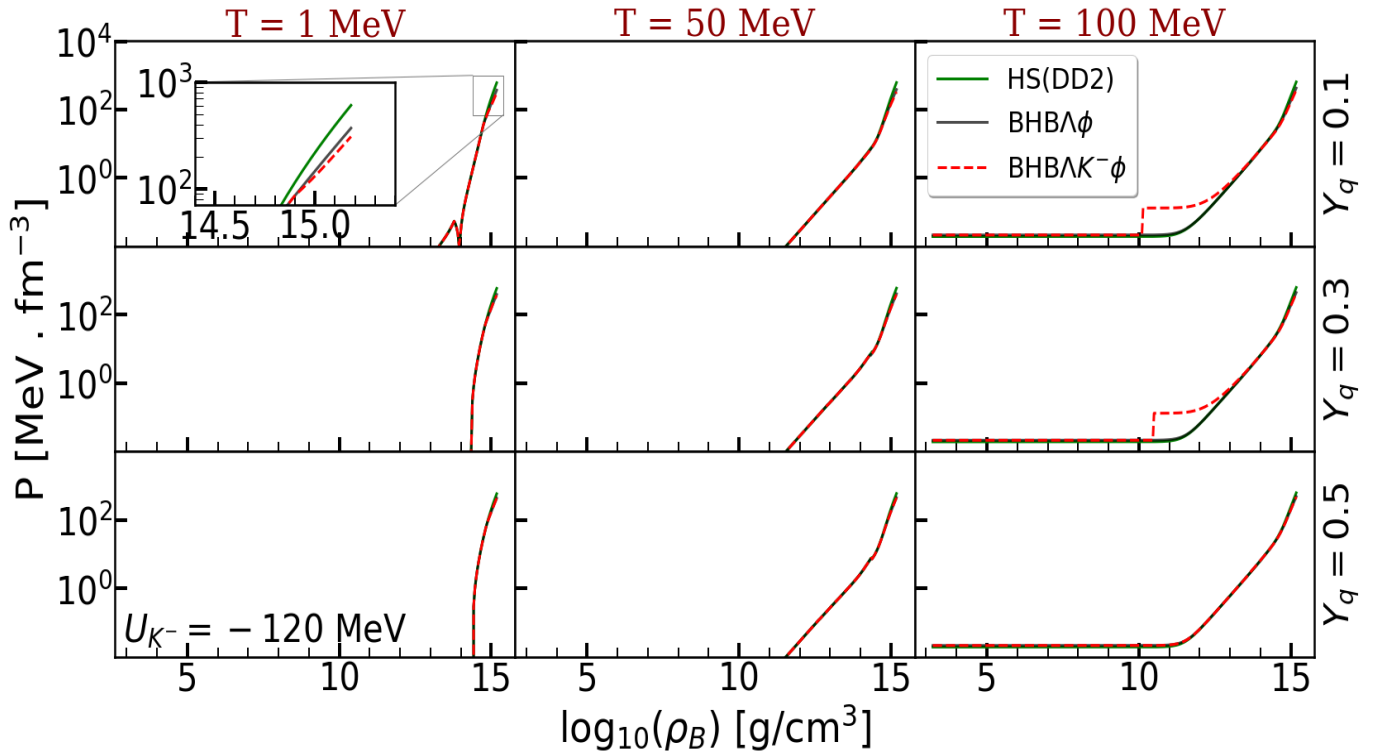


Figure 4. Pressure is shown as a function of baryon mass density for $T=1, 50, 100$ MeV and $Y_q = 0.1, 0.3, 0.5$. Results are shown for three EoSs as depicted in 3. The difference in the EoS at higher density is exhibited in the inset for $Y_q = 0.1$ and $T=1$ MeV.

exhibited a similar phase diagram of nuclear matter with antikaon condensate. Comparing this phase diagram with that of [Malik et al. \(2021\)](#), clearly shows the effect of hyperons. The hyperons visibly delays the kaon condensation to a higher density. Also the critical temperature, above which the K^- condensate dissolves, comes down at a given density. The condensed phase is observed to shrink with higher Y_q , in nuclear as well as hyperon matter; it ceases to exist at all in the presence of hyperons at $Y_q = 0.5$.

4. SUMMARY & CONCLUSION

We have constructed a new EoS table including (anti)kaons and hyperons for core collapse supernova and binary NS merger simulations. We call it HS(DD2) $\Lambda K^- \phi$. The low density, non-uniform matter of this EoS table is generated within an extended version of the NSE model with excluded volume [Hempel & Schaffner-Bielich \(2010\)](#). The uniform matter on the other hand is described in a finite temperature density-dependent relativistic mean field model. The nucleons are described within widely-used meson exchange model using the DD2 parameter set [Typel et al. \(2010\)](#). The interaction between Λ -hyperons is mediated by additional ϕ mesons. It is noted that the fraction of Λ hyperons is significant at ~ 2 times normal nuclear matter density for a cold matter. At higher temperature Λ s populate even at low density matter, their population grows in uniform matter at the cost of neutrons at high density, eventually overshooting neutron fraction at very large density.

We have also considered the role of thermal (anti)kaons and the K^- condensate on the EoS and other thermodynamic observables. At low temperature and low positive charge fraction, the system is populated with K^- condensate and a very small amount of thermal (anti)kaons. However, a high fraction of Λ s at low density does not favour the onset of K^- condensate. At high temperature, only the thermal (anti)kaons populate the matter.

The presence of Λ hyperons, thermal (anti)kaons and the antikaon condensate makes the HS(DD2) $\Lambda K^- \phi$ EoS softest of the nucleon-only HS(DD2) EoS, and the strange matter EoS HS(DD2) $\Lambda \phi$, and the HS(DD2) K^- EoS.

We have shown various thermodynamic observables such as the free energy per baryon, entropy per baryon and pressure of HS(DD2) $\Lambda K^- \phi$ matter as a function of baryon mass density for the set of temperatures, $T = 1, 50, \text{ and } 100$ MeV and positive charge fractions, $Y_q = 0.1, 0.3, \text{ and } 0.5$. For comparison we also plot the corresponding quantities

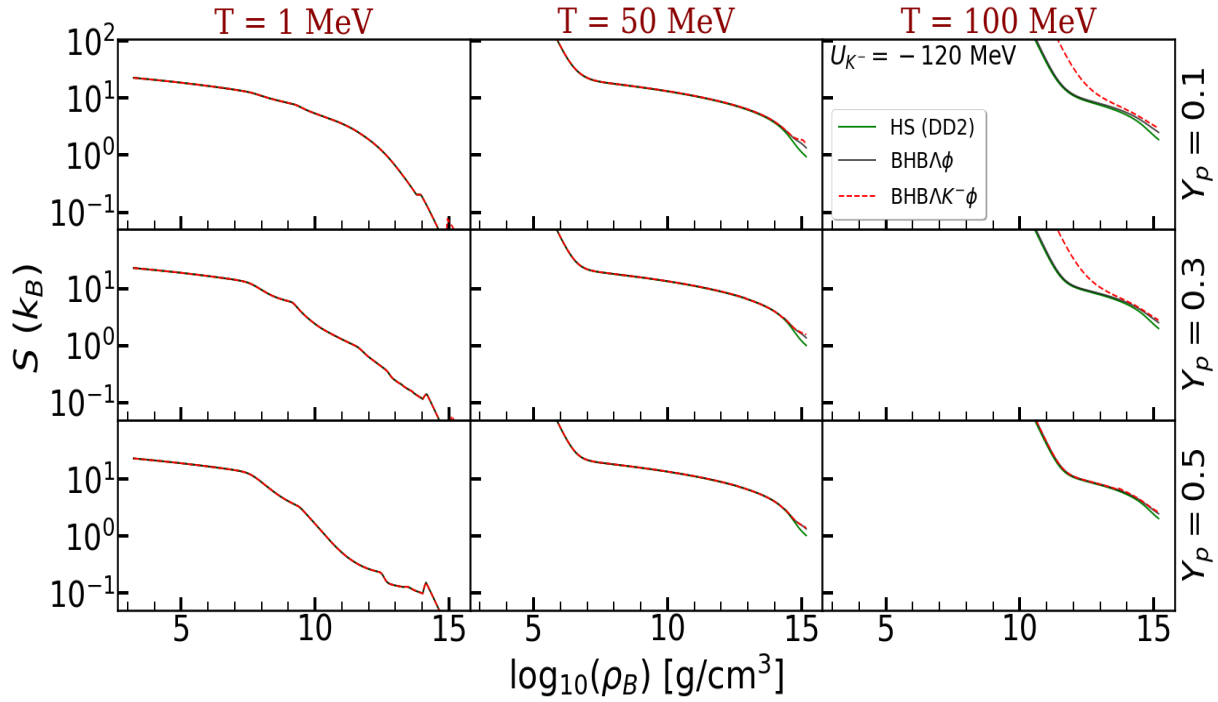


Figure 5. Entropy per baryon is shown as a function of baryon mass density for temperatures $T = 1, 50, 100$ MeV and positive charge fractions $Y_q = 0.1, 0.3,$ and 0.5 . Results from the nucleonic EoS table HS(DD2) (green) and two strange matter EoS tables BHB $\Lambda\phi$ (black) and BHB $\Lambda K^- \phi$ (red dashed) are shown here.

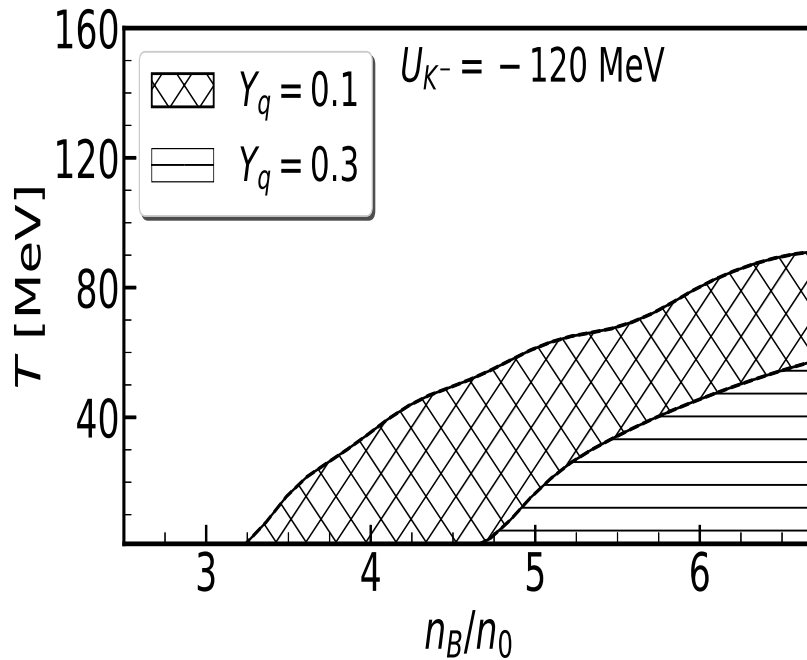


Figure 6. The phase diagram of hyperon matter with antikaon condensate is displayed for $Y_q = 0.1, 0.3,$ and $U_{K^-} = -120$ MeV. The K^- condensed phases, represented by the shaded regions are demarcated from the hadron phases by the solid lines for the two Y_q values.

of HS(DD2) and HS(DD2) $\Lambda\phi$ matter. The effect of the strange particles is mainly observed at high density, that becomes visibly prominent at high temperature.

Finally, we also compute the EoS of the charge neutral and β -equilibrated cold EoS and report the lowering of maximum mass neutron star in the presence of strange particles. The maximum masses are 2.42, 2.24, 2.1 and 2.05 M_{solar} , all are compatible with the heavy neutron stars of masses $\sim 2M_{solar}$, discovered in the past decade [Antoniadis et al. \(2013\)](#); [Cromartie et al. \(2019\)](#). Also, the radii match with the range of radius calculated from the tidal deformability extracted from the BNS merger GW170817 event for a $1.4M_{solar}$ neutron star [Abbott et al. \(2017a\)](#). Recently the Neutron Star Interior Composition Explorer (NICER) observation of PSR J0030+0451 has come up with a radius estimation of $13.02^{+1.24}_{-1.06}$ km for the $1.44M_{solar}$ pulsar PSR J0030+0451 [Miller et al. \(2019\)](#); [Raaijmakers et al. \(2019\)](#). Our results for radius corresponding to $1.4M_{solar}$ neutron star is slightly higher than that of GW170817 [Soma & Bandyopadhyay \(2020\)](#) whereas it is consistent with the NICER observation.

We shall perform supernova simulations and neutron star merger simulations with new HS(DD2) $\Lambda K^- \phi$ EoS table and leave them for a future publication.

APPENDIX

A. DESCRIPTION OF THE TABLE

We follow the format of the widely used, existing supernova EoS tables -Shen [Shen et al. \(1998\)](#) and BHBA ϕ [Banik et al. \(2014\)](#). We arrange the data in a parameter grid of temperature, density and positive charge fraction. The first two parameters have a logarithmic spacing, while the charge fraction is on a linear scale. We group them in blocks of a fixed temperature, starting with the lowest value. Within each temperature block, we group the data according to the positive charge fraction, again starting with lowest values. Finally, for a given temperature and positive charge fraction, we list all the thermodynamic properties according to ascending baryon number densities.

We record only hadronic contributions to different quantities in the table. The contributions of photons, electrons, positrons and neutrinos can be added separately. There are twenty-three entries of the table representing different thermodynamic quantities corresponding to each density grid point in the table. These thermodynamic quantities are listed below.

1. Logarithm of baryon mass density ($\log_{10}(\rho_B)$ [g/cm³]) is defined as the baryon number density multiplied by the value of the atomic mass unit $m_u = 931.49432$ MeV.

2. Baryon number density (n_B [fm⁻³])

3. Logarithm of total positive charge fraction ($\log_{10}(Y_p)$)

4. Total positive charge fraction (Y_p)

5. Free energy per baryon (F) relative to 938 MeV is defined by

$$F = \frac{f}{n_B} - 938. \quad (\text{A1})$$

6. Internal energy per baryon (E_{int}) relative to m_u is defined by

$$E_{int} = \frac{\epsilon}{n_B} - m_u, \quad (\text{A2})$$

where the energy density ϵ is given by Eq.(6).

7. Entropy per baryon (S [k_B]) related to the entropy density through $S = \frac{S}{n_B}$.

8. Average mass number of heavy nuclei (\bar{A}) is defined as $\bar{A} = \sum_{A,Z \geq 6} A n_{A,Z} / \sum_{A,Z \geq 6} n_{A,Z}$

9. Average charge number of heavy nuclei (\bar{Z}) is defined as $\bar{Z} = \sum_{A,Z \geq 6} Z n_{A,Z} / \sum_{A,Z \geq 6} n_{A,Z}$

10. Nucleon effective mass (m^* [MeV])

In the RMF calculation, we use separate values for neutron and proton masses, 939.56536 & 938.27203 MeV respectively. However, the average value of neutron and proton effective masses is stored.

11. Mass fraction of unbound neutrons ($X_n = n_n/n_B$)

12. Mass fraction of unbound protons ($X_p = n_p/n_B$)

13. Mass fraction of unbound Λ s ($X_\Lambda = n_\Lambda/n_B$)

14. Mass fraction of light nuclei (X_a) is defined as $X_a = \sum_{A,Z \leq 5} A n_{A,Z} / n_B$

15. Mass fraction of heavy nuclei (X_A) is defined as $X_A = \sum_{A,Z \geq 6} A n_{A,Z} / n_B$

16. Baryon pressure (P [MeV/fm³])

17. Neutron chemical potential relative to neutron rest mass ($\mu_n - m_n$ [MeV]). Whenever Λ 's are present in the system, $\mu_n = \mu_\Lambda$ condition is satisfied.

18. Proton chemical potential relative to proton rest mass ($\mu_p - m_p$ [MeV])

19. Average mass number of light nuclei (\bar{a}) is defined as $\bar{a} = \sum_{A,Z \leq 5} A n_{A,Z} / \sum_{A,Z \leq 5} n_{A,Z}$

20. Average charge number of light nuclei (\bar{z}) is defined as $\bar{z} = \sum_{A,Z \leq 5} Z n_{A,Z} / \sum_{A,Z \leq 5} n_{A,Z}$

21. Kaon effective mass (m_K^* [MeV])

22. Mass fraction of thermal kaon ($X_K^T = n_K^T/n_B$)

23. Mass fraction of K^- condensate ($X_K^C = n_K^C/n_B$)

Acknowledgements

Authors acknowledge the DAE-BRNS grant received under the BRNS project No.37(3)/14/12/2018-BRNS. DB acknowledges the hospitality at FIAS and support of Alexander von Humboldt Foundation, Germany. The calculations

are performed in the server of Physics Department, BITS-Pilani, Hyderabad Campus.

REFERENCES

- Abbott, B. P., Abbott, R., Abbott, T. D. et al. 2017, *PhRvL*, 119, 161101
- Abbott, B. P., Abbott, R., Abbott, T. D. et al. 2017, *ApJL*, 848 L13
- Abbott, B. P., Abbott, R., Abbott, T. D. et al. 2018, *PhRvL*, 121, 161101
- Abbott, B. P., Abbott, R., Abbott, T. D. et al. 2019, *PhRvX*, 9, 011001
- The LIGO Scientific Collaboration, The VIRGO collaboration, Abbott, B. P., Abbott, R., Abbott, T. D. et al. 2019, *ApJ*, 875, 160
- The LIGO Scientific Collaboration, The VIRGO collaboration, Abbott, B. P., Abbott, R., Abbott, T. D. et al. 2020, *CQGra*, 37, 045006
- Abbott, R., Abbott, T. D., Abraham, S. et al. 2020, *ApJL*, 896 L44
- Antoniadis, J., Freire, P. C. C., Wex, N. et al. 2013, *Science*, 340, 448
- Banik, S. & Bandyopadhyay, D., *Phys. Rev. C*, 64, 055805
- Banik, S., Greiner, W. & Bandyopadhyay, D., *Phys. Rev. C* 78, 065804
- Banik, S. 2014, *Phys. Rev. C*, 89, 035807
- Banik, S., Hempel, M., & Bandyopadhyay, D. 2014, *Astrophys. J. Suppl.*, 214, 22
- Bethe, H. A. & Brown, G. E. 1995, *ApJ*, 445, L129
- Blinnikov, S. I., Panov, I. V., Rudzsky, M. A., & Sumiyoshi, K. 2011, *Astron. Astrophys.* 535, A37
- Buyukcizmeci, N., Botvina, A. S., & Mishustin, I. N. 2014, *Astrophys. J.*, 789, 33
- Char, P. & Banik, S. 2014, *Phys. Rev. C* 90, 015801
- Char P., Banik, S., & Bandyopadhyay, D. 2015, *Astrophys. J.*, 809, 116
- Constantinou, C., Muccioli, B., Prakash, M., & Lattimer, J. M. 2014, *Phys. Rev. C*, 89, 065802
- Cromartie, H. T., Fonseca, E., Ransom, S. M., et al. 2019, *NatAst*, 4, 72
- De, S., Finstad, D., Lattimer, J. M. et al. 2018, *PhRvL*, 121, 091102
- Dover, C. B., & Gal, A. 1985, *Prog. Part. Nucl. Phys.*, 12,171
- Fattoyev, F. J., Piekarewicz, J., & Horowitz, C. J. 2018, *PhRvL*, 120, 172702
- Friedman, E., Gal, A. & Batty, C. J. , *Nucl. Phys. A* 579, 518;
- Batty, C. J., Friedman, E. & Gal, A., *Phys. Rep.* 287, 385
- Friedman, E., Gal, A., Mareš, J. & Cieplý, A., *Phys. Rev. C*, 60, 024314
- Fischer, T., Sagert, I., Pagliara, G., et al. 2011, *Astrophys. J. Suppl. Ser.*, 194, 39
- Fischer, T., Hempel, M., Sagert, I., Suwa, Y., & Schaffner-Bielich, J. 2014, *The European Physical Journal A*, 50, 46
- Glendenning N. K. & Schaffner-Bielich J., *Phys. Rev. D*, 60,025803
- Hebeler, K., Lattimer, J. M., Pethick, C. J., & Schwenk, A. 2013, *Astrophys. J.*, 773, 11
- Hempel, M., & Schaffner-Bielich, J. 2010, *Nucl. Phys. A*, 837, 210
- Hempel, M., Fischer, T., Schaffner-Bielich, J., & Liebendörfer, L. 2012, *Astrophys. J.*, 748, 70
- Hewish, A., Bell, S. J., Pilkington J. D. H. et al. 1968, *Nature*, 217, 709
- Sagert, I., Fischer, T., Hempel, M., Pagliara, G., & Schaffner-Bielich, J. 2009, *Phys. Rev. Lett.*, 102, 081101
- Ishizuka, C., Ohnishi, A., Tsubakihara, K., Sumiyoshi, K., & Yamada, S. 2008, *J. Phys. G*, 35, 085201
- Kaplan, D. B., & Nelson, A. E. 1986, *Phys. Lett. B*, 175,57
- Knorren, R., Prakash, M., & Ellis, P. J. 1995, *Phys. Rev. C*, 52,3470
- Kurkela, A, Fraga, E. S., Schaffner-Bielich, J., & Vuorinen, A. 2014, *Astrophys. J.*, 789, 127
- Lattimer, J. M., & Swesty, F. D. 1991, *Nucl. Phys. A*, 535, 331
- Malik, T., Banik, S. & Bandyopadhyay, D., *The European Physical Journal Special Topics*, 2021 (in press)
- Mares, J., Friedman, E., Gal, A., & Jennings, B. 1995, *Nucl. Phys. A*, 594, 311
- Margalit, B., & Metzger, B. D. 2017, *Astrophys. J. Lett.*, 850, L19
- Millener, D. J., Dover, C. B., & Gal, A. 1988, *Phys. Rev. C*, 38, 2700
- Miller, M. C., Lamb, F. K., Dittmann, A. J. et al. 2019, *ApJL*, 887, L24
- Most, E. R., Weih, L. R., Rezzolla, L., & Schaffner-Bielich, J. 2018, *PRL*, 129, 261103
- Nakazato, K., Furusawa, S., Sumiyoshi, K., et al. 2012 *Astrophys. J.*, 745, 197
- Nakazato, K., Sumiyoshi, K., & Yamada, S. 2008, *Phys. Rev. D*, 77, 103006 2018, *PhRvL*, 120, 261103

- Oertel, M., Fantina, A. F., & Novak, J. 2012, *Phys. Rev. C*, 85, 055806
- Oertel, M., Hempel, M., Klähn, T., & Typel, S. 2017, *Rev. Mod. Phys.*, 89, 015007
- Lope Oter, E., Windisch, A., Llanes-Estrada, F. J., & Alford, M. 2019, *J. Phys. G*, 46, 084001
- Peres, B., Oertel, M., & Novak, J. 2013, *Phys. Rev. D*, 87, 043006
- Pons, J. A., Reddy, S., Ellis, P. J., Prakash, M., & Lattimer, J. M. 2000, *Phys. Rev C*, 62, 035803
- Raaijmakers, G., Riley, T. E., Watts, A. L. et al. 2019, *Astrophys. J. Lett.*, 887, L22
- Raduta, Ad. R., & Gulminelli, F. 2010, *Phys. Rev. C*, 82, 065801
- Radice, D., Perego, A., Hotokezaka, K., Fromm, S. A., Bernuzzi, S., & Roberts, L. F. 2018, *Astrophys. J.*, 869, 130
- Raithel, C., Özel, F., & Psaltis, D. 2018, *Astro. Phys. J.*, 857, L23
- Rezzolla, L., Most, E. R., & Weih, L. R. 2018, *Astrophys. J. Lett.*, 852, L25
- Riley, T. E., Watts, A. L., Bogdanov, S. et al. 2019, *ApJL*, 887, L21
- Romani, R. W., Kandel, D., Filippenko, A. V. et al., 2021, *ApJL*, 908, L46
- Ruiz, M., Shapiro, S. L., & Tsokaros, A. 2018, *Phys. Rev. D*, 97, 021501
- Schaffner, J., Stöcker, H., & Greiner, C. 1992, *Phys. Rev. C*, 46, 322
- Schaffner, J., & Mishustin, I. N. 1996, *Phys. Rev. C*, 53, 1416
- Shen, H., Toki, H., Oyamatsu, K., & Sumiyoshi, K. 1998, *Nucl. Phys. A*, 637, 435
- Shen, G., Horowitz, C. J., & Teige, S. 2010, *Phys. Rev. C*, 82, 045802
- Shen, G., Horowitz, C. J., & Teige, S. 2011b, *Phys. Rev. C*, 83, 035802
- Shen, G., Horowitz, C. J., & O'Connor, E. 2011a, *Phys. Rev. C*, 83, 065808
- Shen, H., Toki, H., Oyamatsu, K., & Sumiyoshi, K. 2011c, *Astrophys. J. Suppl. Ser.*, 197, 20
- Shibata, M., Fujibayashi, S., Hotokezaka, K. et al. 2017, *PhRvD*, 96, 123012
- Shibata, M., Zhou, E., Kiuchi, K., & Fujibayashi, S. 2019, *Phys. Rev. D*, 100, 023015
- Steiner, A., Hempel, M., & Fischer, T. 2013, *Astrophys. J.*, 774, 17
- Sumiyoshi, K., Ishizuka, C., Ohnishi, A., Yamada, S., & Suzuki, H. 2009, *Astrophys. J.*, 690, L43
- Togashi, H., Takano, H., Sumiyoshi, K., & Nakazato, K. 2014, *Prog. Theor. Exp. Phys.*, 023D05
- Typel, S., Oertel, M., Klähn, T. 2013, *arXiv:1307.5715*
- Tólos, L., Ramos, A. & Oset, E., *Phys. Rev C*, 74, 015203
- Tolos, L. & L. Fabbietti, L., *Prog. Part. Nucl. Phys.* 112, 130770
- Typel, S., & Wolter, H. H. 1999, *Nucl. Phys. A*, 656, 331
- Typel, S., Röpke, G., Klähn, T., Blaschke, D., & Wolter, H. H. 2010, *Phys. Rev. C*, 81, 015803
- Soma S., & Bandyopadhyay D., *Astrophys. J.*, 890, 139
- Zhao, T. & Lattimer, J. M. 2018, *Phys. Rev. D*, 98, 063020